Faraday Discussions

ARTICLE

Towards a 3D GeSbTe Phase Change Memory with integrated selector by non-aqueous electrodeposition

Ruomeng Huang[a], Gabriela P. Kissling[b], Reza Kashtiban[c], Yasir J. Noori [a], Katarina Cicvarić[a], Wenjian Zhang[b], Andrew L. Hector[b], Richard Beanland[c], David C. Smith[d], Gillian Reid[b], Philip N. Bartlett[b] and C. H. "Kees" de Groot*[a]

Received 00th January 20xx,
Accepted 00th January 20xx
DOI: 10.1039/x0xx00000x

We have recently reported a new method for electrodeposition of thin film and nanostructured phase change memory (PCM) devices from a single, highly tuneable, non-aqueous electrolyte. The quality of the material was confirmed by phase cycling *via* electrical pulsed switching of both 100 nm nano-cells and thin film devices. This method potentially allows deposition into extremely small confined cells down to less than 5 nm, 3D lay-outs that require non-line-of-sight techniques, and seamless integration of integrated selector devices. As electrodeposition requires a conducting substrate, the key condition for electronic applications based on this method is the use of patterned metal lines as the working electrode during the electrodeposition process. In this paper we show design and fabrication of a 2D passive memory matrix in which the word lines act as the working electrode and nucleation site for the growth of confined cells of Ge-Sb-Te. We will discuss the precursor requirement for deposition from non-aqueous, weakly coodinating solvents, show transmission electron microscopy analysis of the electrodeposition growth process and elemental distribution in the deposits, and the fabrication and characterisation of the Ge-Sb-Te memory matrix.

Introduction

Phase change memory technology is a mature technology, but significant scaling is required to achieve the required density for killer applications in either the memory-storage space or in neuromorphic computing.[1–3] Conventional 'mushroom' phase change device structures suffer from thermal cross-talk between adjacent cells[4] and confined cells are therefore more favourable for high density scaling as it could reduce the thermal cross-talk and simultaneously reduce the currents required for the switching operations.[3] Conventional deposition of phase change materials by physical vapour deposition (PVD) does not allow selective deposition and is unable to uniformly fill small cells with medium to high aspect ratio. Hence, other deposition approaches have had to be investigated in the last 10 years, including chemical vapour deposition (CVD), atomic layer deposition (ALD) and electrodeposition.[5–7]

Electrodeposition is a well-established material preparation approach in the electronics industry.[8,9] The bottom-up nature of electrodeposition makes it a promising technique to deposit materials selectively into conductive nanoscale holes. Several attempts have been made to deposit phase change materials by electrodeposition and binary chalcogenides, such as Sb_2Te_3 and Bi_2Te_3 were successfully deposited.[7,10] However, the electrodeposition of $Ge_2Sb_2Te_5$ is significantly more difficult. The main issue being the rather extreme conditions required for the electrodeposition of Ge; when deposited from aqueous systems, the Ge deposition occurs at similar potentials to hydrogen evolution, leading to bubble formation.[11] This makes the controlled preparation of alloys challenging and aqueous electrodeposition of Ge-Sb-Te will not have the required freedom in parameter space to reach the required

[a] School of Electronics and Computer Science, University of Southampton, Southampton, SO17 1BJ, UK. E-mail: r.huang@soton.ac.uk; C.H.de-Groot@soton.ac.uk
[b] School of Chemistry, University of Southampton, Southampton, SO17 1BJ, UK.
[c] Department of Physics, University of Warwick, Coventry CV4 7AL, UK.
[d] School of Physics and Astronomy, University of Southampton, Southampton, SO17 1BJ, UK.

stringent optimisation for non-volatile memory. In our recent paper we presented an electrodeposition method based on a novel non-aqueous electrolyte.[12] The electrodeposition of phase change alloys becomes accessible thanks to suitably tailored, highly soluble precursor compounds containing the relevant elements. The non-aqueous electrolyte has a wider electrochemical window than water, facilitating the deposition of Ge, and allowing us to demonstrate cycling of electrodeposited Ge-Sb-Te phase change memory in 100 nm confined cells.

This paper is organised as follows. In the next section, "Electrodeposited Phase Change Memory", we will show our previous results on the electrical characteristics of thin film and confined nano-cells of Ge-Sb-Te phase change memory,[12] now supported by a detailed transmission electron microscopy analysis of the composition and elemental distribution of the confined cells. The "Non-aqueous Electrodeposition from Non-Coordinating Solvents" section, will explain the rationale behind the solvent, electrolyte and precursor selection. The control capabilities of this system for both thin films and confined cells will be demonstrated through a series of experiments in which the Ge precursor content in the solution has been systematically increased. In the "Electrodeposited Passive Memory Matrix" section, we will show that it is possible to design a functional integrated circuit in which the word lines of the memory matrix act as the working electrode for the growth of the electrodeposited Ge-Sb-Te memory cells. It is shown that the ohmic drop in the word lines is sufficiently small such that it does not significantly affect the electrodeposition potential and that this value is scale independent. Initial characterisation of the memory cells is presented. The paper will end with a "Discussion and Conclusion" section which will contain ideas for passive memory matrix scaling that are uniquely or particularly suitable for electrodeposition techniques such as gradient compositional growth to counteract electro-migration, integration of chalcogenide based ovonic threshold selector devices, and non-line-of-sight 3-dimensional growth techniques.

Electrodeposited Phase Change Memory

Electrical characteristics of thin films and confined cells

The electrical memory switching properties of the electrodeposited Ge-Sb-Te thin films and confined nanocells were investigated by fabricating vertical memory devices (Fig. 1).[12] The fabrication was undertaken by either patterning the top TiN electrode directly on the Ge-Sb-Te thin film (Fig. 1a) or filling etched SiO_2 nanoholes with Ge-Sb-Te by electrodeposition on TiN bottom electrodes and subsequently patterning the top TiN electrode (Fig. 1b). The switching behaviour observed was reproducible for a large number of different devices. The phase change switching performance of a GST thin film device was characterised with a V_{set} pulse of 2 V/ 1 ms and a V_{reset} pulse of 6 V/ 200 ns. A stable switching over 180 cycles was achieved without failure, while the ON/OFF resistance ratio was maintained at three orders of magnitude as shown in Fig. 1b. Fig. 1d illustrates programming and erase cycles of a 100 nm GeSbTe memory cell switched between high- and low-resistance states repeatedly with nearly two orders of magnitude difference between amorphous and crystalline state.

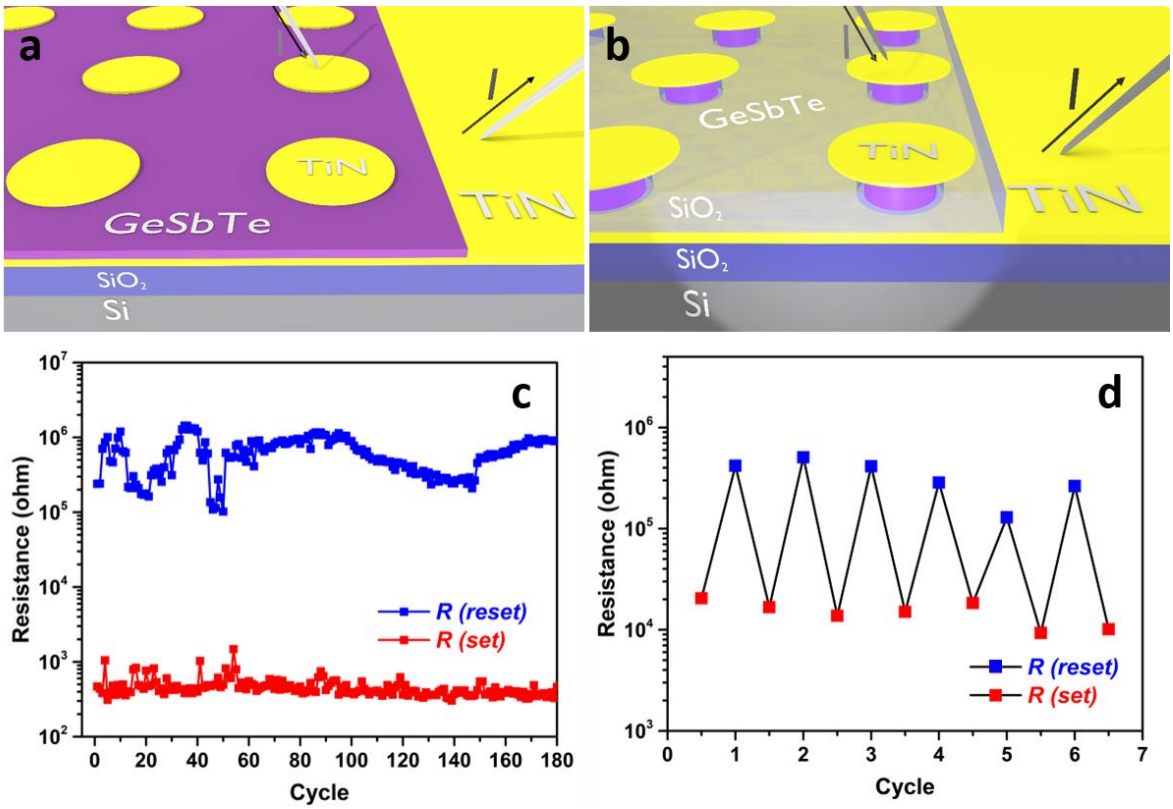

Fig. 1. Schematic of (a) thin film and (b) nanoscale phase change memory; Resistive switching cycling behaviours of of (c) thin film and (b) nanoscale Ge-Sb-Te phase change memory fabricated by non-aqueous electrodeposition. Reproduced from Ref. 12 with permission from the Royal Society of Chemistry.

Device characterisation using electron microscopy

A combination of non-destructive scanning electron microscopy (SEM) and energy dispersive X-ray analysis (EDX) was employed to characterise the composition and morphology of the electrodeposited devices as shown in Fig. 2. The electrodeposited Ge-Sb-Te film is characterised by small granules with noticeably irregular nucleation on the surface (Fig. 2a). The composition of the film is found to be Ge 24(2)-Sb 20(3)-Te 56(3). On the other hand, electrodeposition of Ge-Sb-Te into confined nanocells resulted in a uniform overfilling of all cells, suggesting homogeneous electrochemical growth (Fig. 2b). However, top-view EDX on a single nanocell reveals a composition of Ge 12(3)-Sb 66(3)-Te 22(1). This extracted Ge-Sb-Te composition is significantly different from the (intended) GST225 composition which has been previously established for a thin film from the same solution. Despite this large deviation from the GST225 composition and the Sb_2Te_3-GeTe tie line, the cell's behaviour is not too dissimilar from the thin film. As has been established by multiple authors over the last years, the range in the ternary compositional diagram which demonstrate phase change memory behaviour is surprisingly large.[13,14] In the next section, we will show the possibility to control the nanostructured confined cell composition by variation in precursor concentration.

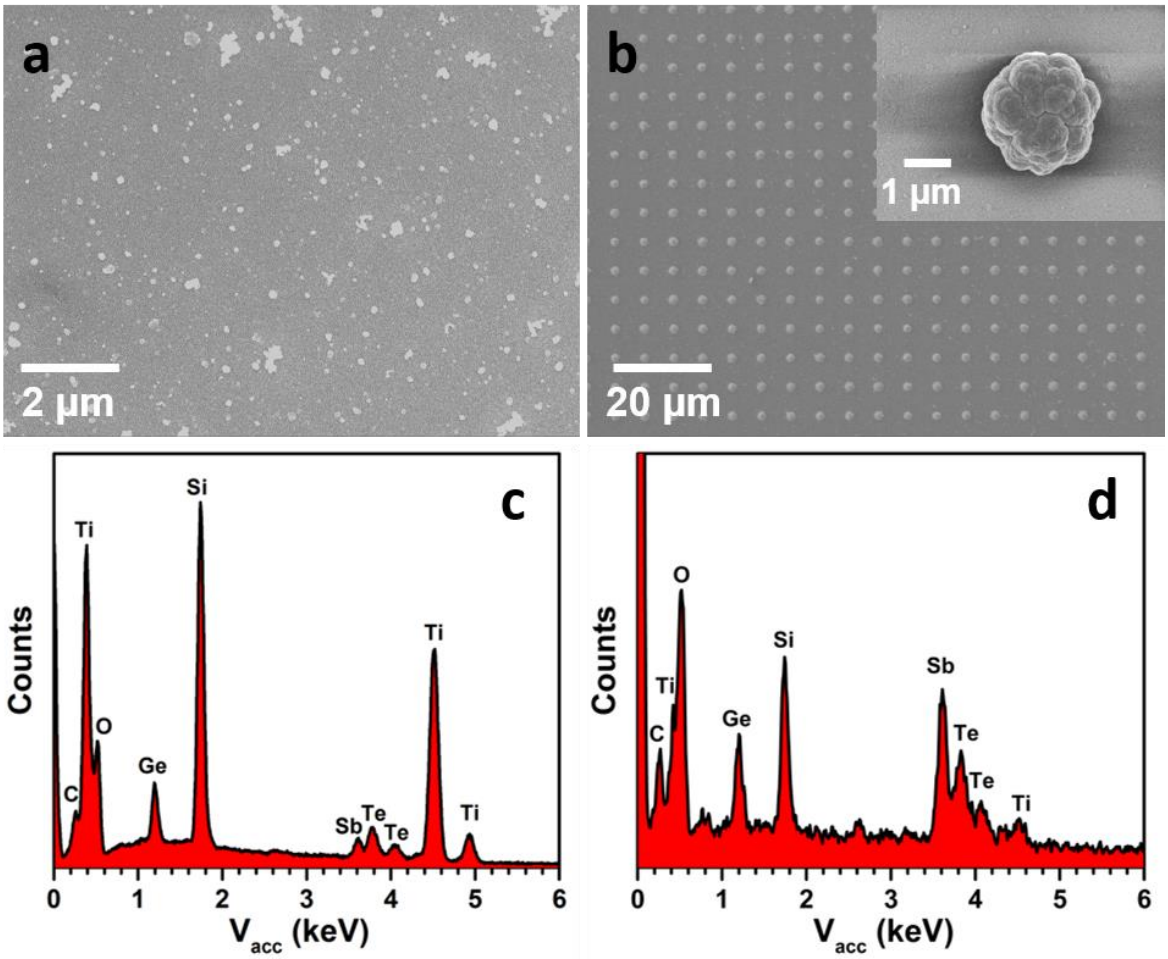

Fig. 2 SEM images and EDX spectra of an electrodeposited Ge-Sb-Te thin film (a and c) and confined cells (b and d). The samples were obtained from electrolytes containing 1 mM $[NBu^n_4][GeCl_5]$, 1 mM $[NBu^n_4][SbCl_4]$ and 2 mM $[NBu^n_4]_2[TeCl_6]$ in 0.1 M $[NBu^n_4]Cl$ in CH_2Cl_2. The TiN substrates acted as the working electrodes. A Pt gauze and an Ag/AgCl (0.1 M $[NBu^n_4]Cl$ in CH_2Cl_2) electrode were used as counter and reference electrodes. A deposition potential of -1.75 V *vs.* Ag/AgCl was used for both deposits.

Non-aqueous Electrodeposition

Precursor chemistry for electrodeposition from weakly coordinating solvents

An electrolyte system has been developed based on tetrabutylammonium chlorometallate salts dissolved in CH_2Cl_2 (dichloromethane) under inert atmosphere conditions. These well-defined and easily synthesised reagents show very high solubility in organic solvents, allowing the preparation of high-concentration electrolytes. The low surface tension of CH_2Cl_2 also makes it a promising solvent for the electrodeposition of materials into nano-patterned substrates. The presented precursor complexes are chemically very similar salts and mutually compatible in solution, allowing alloyed materials to be obtained by combining the relevant chlorometallates. The electrolyte system prepared from the tetrabutylammonium chlorometallates ($[NBu^n_x]_y[MCl_z]$ with tetrabutylammonium chloride $[NBu^n_4]Cl$ as the supporting electrolyte, proved suitable for the electrodeposition of a wide variety of p-block elements including selenium, indium, antimony, tellurium, germanium and bismuth, as demonstrated previously.[15] The electrodeposition of further p-block metals and metalloids may also be feasible using a similar approach if the corresponding chlorometallate salts can be formed.

Fig. 3a shows a schematic of the electrodeposition set-up. GeSbTe films were deposited from a range of electrolytes containing various amounts of the Ge precursor. GeSbTe films were deposited onto TiN from an electrolyte

containing **X** mM $[NBu^n_4][GeCl_5]$ (X = 0, 1, 4, 7, 10), **1** mM $[NBu^n_4][SbCl_4]$ and **2** mM $[NBu^n_4]_2[TeCl_6]$. 0.1 M $[NBu^n_4]Cl$ was added to the CH_2Cl_2 as a supporting electrolyte. The deposition potential was fixed at -1.75 V *vs*. Ag/AgCl. In electrodeposition there is a direct relationship between the current passed through the cell and the amount of material deposited, which is solely determined by the oxidation state of the atom in the precursor (Ge^{+4}, Sb^{+3}, Te^{+4}). Using the relative atomic mass of the deposited material (3308.2 g/mol for GST225) and the appropriate density (5300 kg/m^3 for the amorphous phase), deposition ratio b = 5.9x10^{-11} m^3/C is estimated Minor variations in this calculation are valid for different compositions. The film thickness is controlled to around 200 nm by charge control.

Fig. 3b shows cyclic voltammograms recorded in the electrolytes with varying Ge concentrations. There are a few apparent changes when adding the germanium to the electrolyte: a new cathodic peak appears at around -0.1 V. This peak is associated with an initial reduction of the Ge^{IV} compound to Ge^{II} and was seen in various pure germanium electrolytes as well.[16–18] The germanium is not reduced to Ge^0 at this stage and no deposition takes place although Faradaic current is present. In addition, the two peaks due to antimony and tellurium that are present without germanium (c2 and c3) shift significantly towards more cathodic potentials upon addition of germanium. A fourth cathodic peak (c4) also appears at around -1.75 V which is due to the germanium reduction to Ge^0. At this potential all three elements are depositing and the relative deposition rates can be varied by precursor concentration variation. When looking at the reverse scan direction in the cathodic region the current drops to zero at more cathodic potentials in the presence of germanium. In the anodic region a clear change can be observed. While there is a significant stripping signal in the absence of germanium, there is hardly any stripping observed in the presence of germanium.

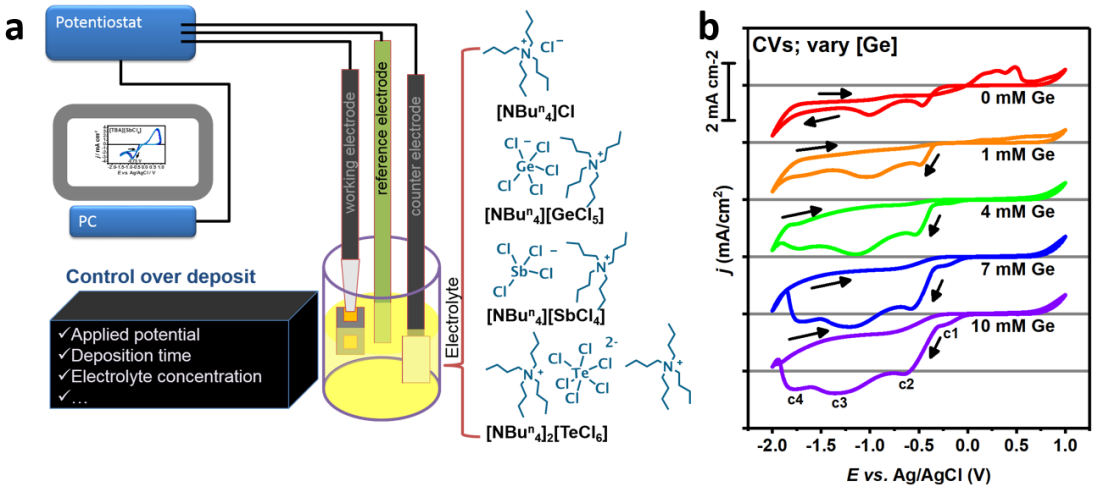

Fig. 3 (a) Schematic of the electrodeposition setup; (b) Cyclic voltammograms for Ge-Sb-Te electrolytes containing 0, 1, 4, 7 or 10 mM $[NBu^n_4][GeCl_5]$ 1 mM $[NBu^n_4][SbCl_4]$ and 2 mM $[NBu^n_4]_2[TeCl_6]$ in dichloromethane containing 0.1 M $[NBu^n_4]Cl$ as the supporting electrolzte. Glassy carbon electrodes were used as the working electrodes. A Pt gauze and an Ag/AgCl (0.1 M $[NBu^n_4]Cl$ in CH_2Cl_2) electrode were used as counter and reference electrodes. The voltammograms were recorded at 50 mV/s.

Thin film composition and morphology of electrodeposited Ge-Sb-Te

The morphology of the deposited films is shown in Fig. 4. A clear decrease in the roughness can be observed with increasing Ge precursor amount in the electrolyte. The 0 mM Ge electrolyte produced a deposit that appears to be discontinuous with only clusters formed on the TiN electrode. This suggests that pure SbTe has a strong preference for self-growth over growth on TiN leading to large grains and clustering. Even small amounts of Ge (in the

electrolyte and the actual deposit) resulted in continuous films, even though clusters can still be observed on the film for low Ge precursor concentrations.

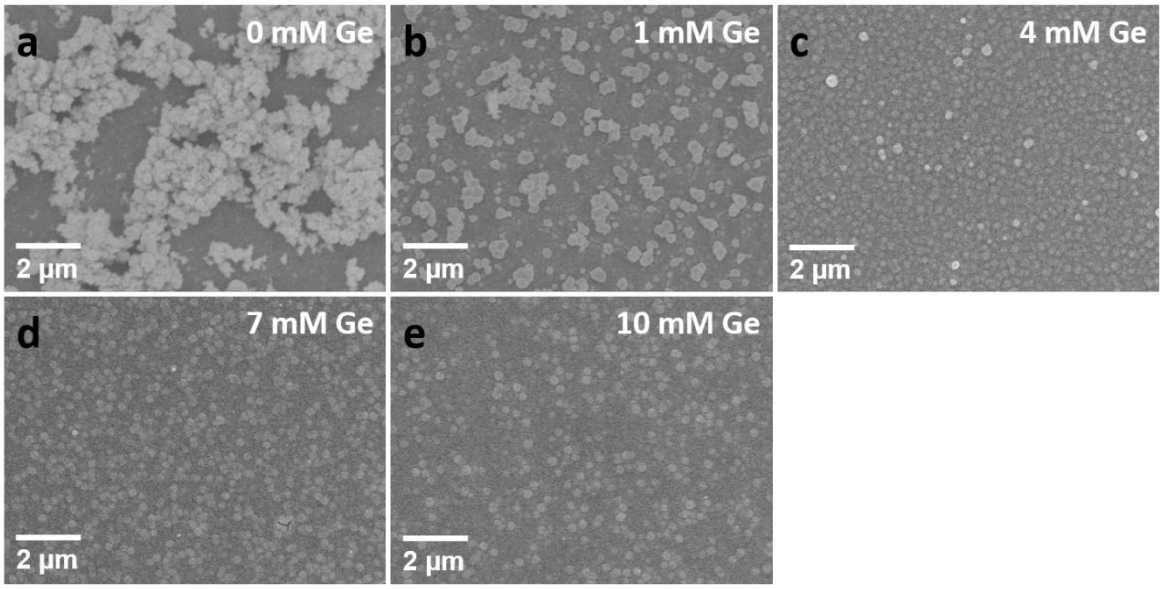

Fig. 4 SEM images of the as-deposited films on TiN prepared in electrolytes containing (a) 0, (b) 1, (c) 4, (d) 7 or (e) 10 mM $[NBu^n_4][GeCl_5]$, 1 mM $[NBu^n_4][SbCl_4]$ and 2 mM $[NBu^n_4]_2[TeCl_6]$ in 0.1 M $[NBu^n_4]Cl$ in CH_2Cl_2. A Pt gauze and an Ag/AgCl (0.1 M $[NBu^n_4]Cl$ in CH_2Cl_2) electrode were used as counter and reference electrodes. The deposition potential was held at -1.75 V and a charge of -0.05 C was passed to obtain deposits with a controlled thickness.

The decrease in the roughness was further confirmed by atomic force microscopy (AFM) measurements (shown in Fig. 5). Note that the measurement on the film obtained in the electrolyte with 0 mM Ge was not possible due to the discontinuity and abruptness of the film. For the film obtained with 1 mM Ge in the electrolyte, the root mean square (RMS) roughness was found to be 264 nm. This high value of roughness is likely due to the existence of the large clusters on top of the film. These clusters also lead to tip-artefacts and the exact value of the RMS roughness might be unreliable. With increasing Ge precursor concentration in the electrolyte, the RMS roughness value reduces to 26 nm. A sputtered GST225 film was also measured as a reference and the RMS was found to be 5 nm.

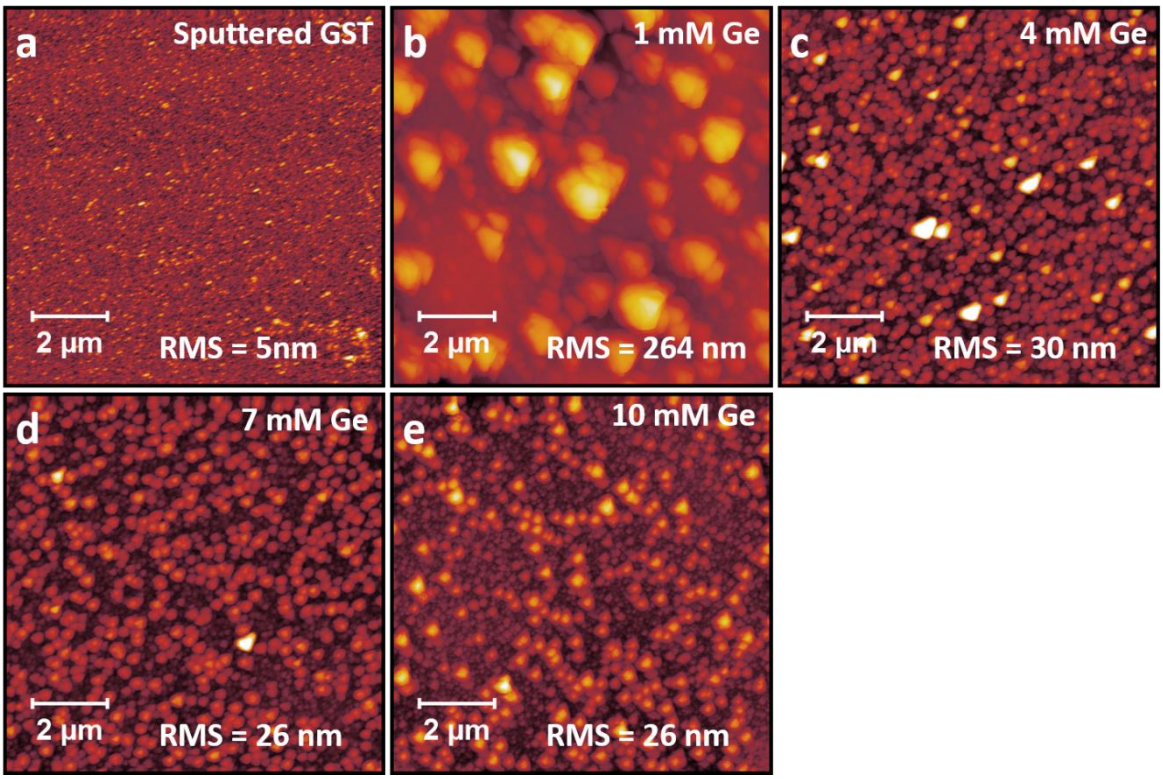

Fig 5 AFM images of (a) sputtered GST and of films deposited in electrolytes containing (b) 1, (c) 4, (d) 7 or (e) 10 mM $[NBu^n_4][GeCl_5]$, 1 mM $[NBu^n_4][SbCl_4]$ and 2 mM $[NBu^n_4]_2[TeCl_6]$ in 0.1 M $[NBu^n_4]Cl$ in CH_2Cl_2. A Pt gauze and an Ag/AgCl (0.1 M $[NBu^n_4]Cl$ in CH_2Cl_2) electrode were used as counter and reference electrodes. The deposition potential was held at -1.75 V and a charge of -0.05 C was passed to obtain deposits with a controlled thickness.

The compositions of the films were studied by EDX spectroscopy. An increased atomic percentage of Ge was observed in the films deposited from the electrolytes containing more Ge precursor concentrations, except for the deposit obtained in the electrolyte containing 10 mM $[NBu^n_4][GeCl_5]$ (shown in Fig. 6a). This is accompanied by a decrease in the Sb in the deposits. However, it is worth mentioning that signals from Ge, Sb and Te elements are relatively weak (<3%) in these EDX measurements. Hence the compositions need to be treated with caution.

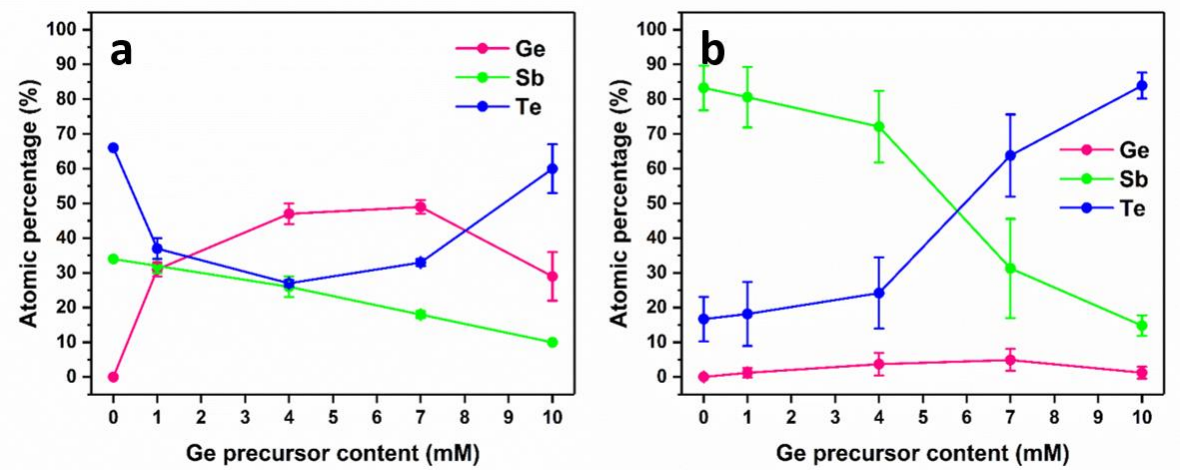

Fig. 6 Compositions of Ge-Sb-Te (a) films and (b) nanocells in 100 nm confined cells deposited from electrolytes containing 0, 1, 4, 7 or 10 mM $[NBu^n_4][GeCl_5]$, 1 mM $[NBu^n_4][SbCl_4]$ and 2 mM $[NBu^n_4]_2[TeCl_6]$ in 0.1 M $[NBu^n_4]Cl$ in CH_2Cl_2. A Pt gauze and an Ag/AgCl (0.1 M $[NBu^n_4]Cl$

in CH_2Cl_2) electrode were used as counter and reference electrodes. The deposition potential was held at -1.75 V. For the thin films (a) a 200 nm thin film thickness was attempted by setting a deposition charge of -0.05 C. A deposition time of 10 s was passed to obtain well-formed nanocells (b). The connect lines are guides of eye.

Nanostructured cell composition and morphology of electrodeposited Ge-Sb-Te

A systematic compositional analysis of the cells was performed both by top down SEM/EDX and cross-sectional STEM-EDX analysis. The composition of the GeSbTe in the nanocell electrodeposited from electrolytes with varying Ge precursor concentration was characterised by top-down SEM. In general, all the nanocells were extremely Ge deficient as shown in Fig. 6b. The Ge content of the deposits never increased above 5 %. Interestingly, whilst the samples obtained from electrolytes with lower concentrations of Ge were Sb rich, the deposit obtained from the electrolyte with the highest Ge concentrations were very Te rich. Similar to the thin films, the Sb composition decreases with increasing Ge precursor concentration in the electrolyte.

The variation in the Ge precursor concentration is demonstrated to have a strong and non-linear effect on both the thin film composition and the nanostructured cells. For both the former and the latter, it is observed that Ge precursor concentration increase has a minor effect on the actual amount of Ge in the solid state product while, more unexpectedly, it has a dramatic effect on the Sb/Te ratio, particularly in the nanostructured templates. It is clear that variation in Ge precursor concentration is only a very small step into the full parameter space that can be reached with electrodeposition. The effect of deposition potential has been addressed in our previous work,[19] whereas absolute concentration (not only relative ratios) of each precursor is also shown to have a significant influence. Factors, such as pre-pulsing, initial nucleation, levellers, series resistance, and surface and loading effects have not yet been investigated. Electrodeposition of functional semiconducting alloys and compounds is definitely still in its infancy, but the initial successful results we summarised above are a first major step towards its exploitation.

Destructive focused ion beam (FIB) sectioning with transmission electron microscopy (TEM) and STEM-EDX measurements have been employed to characterise the composition and morphology of individual electrodeposited nanocells. The sample was imaged and analysed by means of STEM-EDS in doubly corrected JEOL ARM200F TEM equipped with a 1000TLE windowless Oxford Instruments spectrometer. In Fig. 7 we show cross-sectional TEM and STEM-EDX images of a device in which GeSbTe has been electrodeposited into a 100 nm cell without a top contact, from an electrolyte containing 4 mM of $[NBu^n_4][GeCl_5]$, 1 mM $[NBu^n_4][SbCl_4]$ and 2 mM $[NBu^n_4]_2[TeCl_6]$. The deposit has the form of a mushroom with a stalk defined by the cell and a domed overfilling. The deposit is reasonably uniform apart from an enhancement of the Te content at the surfaces of the “mushroom cap”.

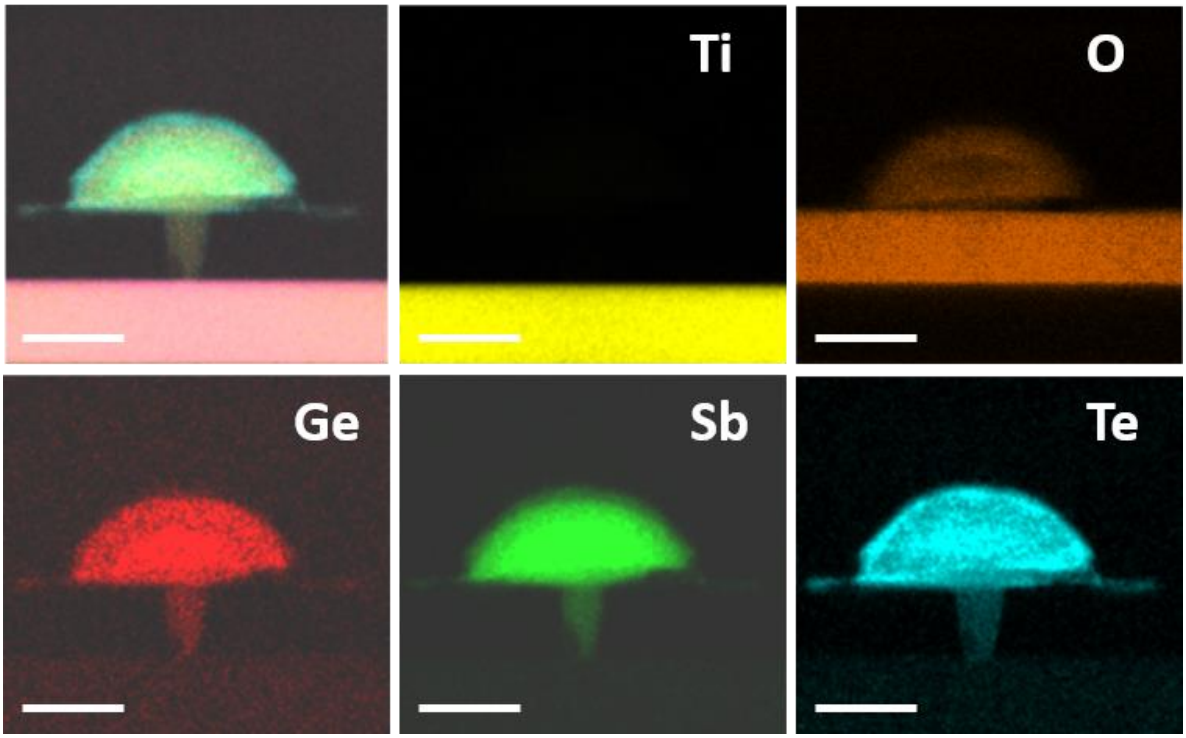

Fig. 7 Cross-sectional STEM-EDX on 100nm confined cell Ge-Sb-Te phase change memory prepared from an electrolyte containing 4 mM $[NBu^n_4][GeCl_5]$, 1 mM $[NBu^n_4][SbCl_4]$ and 2 mM $[NBu^n_4]_2[TeCl_6]$. A Pt gauze and an Ag/AgCl (0.1 M $[NBu^n_4]Cl$ in CH_2Cl_2) electrode were used as counter and reference electrodes. The deposition potential was held at -1.75 V for 10 s.The scale bar is 250nm.

The composition of the nanoscale confined cell extracted from these measurement is presented in Table 1. The composition of Ge-Sb-Te thin films electrodeposited from the same electrolyte is also included for comparison. Whilst it is possible that sample geometry dependent X-ray re-absorption effects could affect the composition measured using EDX, comparison of SEM-EDX and TEM-EDX measurements on the same device suggest this is not a significant problem. The results show that the amount of Te is much smaller in the stalk of the nanocell than in the overfill and the amount of germanium is highest at the base of the stalk. The sample is Sb-rich throughout the stalk and becomes Te-rich in the cap. The data presented show that the Ge concentration decreases from approximately 10% at the stalk to around 5% at the top of the mushroom. The Te concentration on the other hand increases from only 10% at the base of the mushroom to around 60% on the surface of the mushroom cap. The antimony concentration is high in the stalk (*ca.* 80%) and lower on the surface of the cap (*ca.* 35%)

Table 1. EDX compositional analysis of cross-sectional STEM/EDX and top view SEM/EDX of Ge-Sb-Te cells prepared from a solution with 4 mM $[NBu^n_4][GeCl_5]$,1 mM $[NBu^n_4][SbCl_4]$ and 2 mM $[NBu^n_4]_2[TeCl_6]$. A Pt gauze and an Ag/AgCl (0.1 M $[NBu^n_4]Cl$ in CH_2Cl_2) electrode were used as counter and reference electrodes. The deposition potential was held at -1.75 V for 10 s.

Element %	Electrolyte	Thin film SEM-EDX	Nanocell SEM-EDX	Nanocell-stalk STEM-EDX	Nanocell-overfill STEM-EDX
Ge	58(1)	50(5)	5(5)	10(5)	5(5)
Sb	14(1)	25(5)	70(15)	80(10)	35(20)
Te	28(1)	25(5)	25(20)	10(5)	60(20)

Electrodeposited Passive Memory Matrix

Passive memory matrix design for electrodeposition

The key requirement in electrodeposition which sets it apart from PVD and CVD, is the necessity of a conducting substrate. This might be advantageous enabling particular design features, but it also is a limiting factor. Electrodeposition when not using a conducting top layer (such as in the dual damascene process[8]) has been limited to large area contacts with multiple devices in parallel. This is akin to making transistors with a single back contact which allows simple characterisation for research purposes, but is not suitable for actual applications. There is hence a strong requirement to show that patterned back contacts can be used such that each electrodeposited cell is individually addressable. Here we demonstrate the feasibility of a dense matrix design for non-volatile memory. We will firstly present our design, and in the next section, demonstrate that the design satisfies the requirement of minimum resistance/ohmic drop across the working electrode.

The device structure is illustrated in Fig. 8. A good electrical connection (short) must be made between a large contact window which connects to the potentiostat and each individual word line during electrodeposition, while during electrical operation each word line has to be individually addressable (open). This conundrum is solved by cleaving the chip after electrodeposition across the connection bus, thereby severing each individual word line. In this design with many small matrices, this process is slightly inefficient in terms of space requirements, but for a single matrix per chip the overhead is small. An alternative approach which has recently been demonstrated for 50 μm^2 electrodeposited Bi_2Te_3 thermo-electric generators, is severance of electrodeposited contacts by ion beam milling.[20]

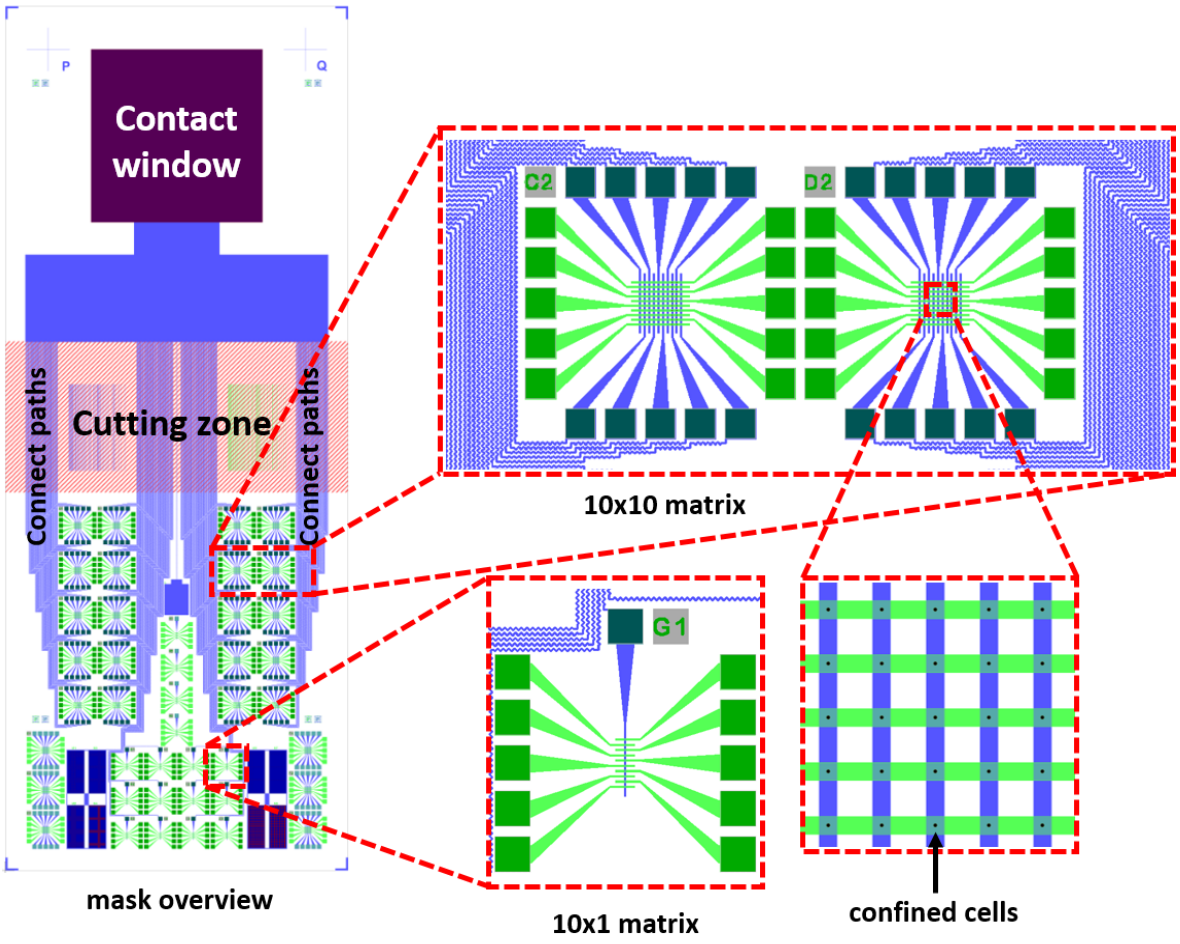

Fig. 8 Design of passive matrix suitable for electrodeposition with lithographically defined working electrode (left) and functional 10x10 and 10x1 passive matrix cell with e-beam lithography confined cells.

The relatively long word lines that provide contact to each individual cell cause an significant ohmic voltage drop (V_{drop}). In a first approximation, the line resistance *R* is proportionate to the length/width (*l*/*w*) of the line and the TiN sheet resistance $R_{\square} = \rho/t$ with *t* the thickness of the TiN bottom electrode. The electrodeposition current *i* is the current density *j* times the area $A = nd^2$, where *n* is the number of cells on a word line and *d* the cell dimension. Aggressively scaled, *n* approaches *l*/*w* and *d* = *w*. This results in the very simple and elegant expression for $V_{drop} = jl^2R_{\square}$. The voltage drop is independent of the scaling of the line width and is roughly similar for both thin film deposition and nanostructured lines:

$$\boldsymbol{V_{drop} = iR = jAR = jA\frac{\rho l}{tw} = jA\frac{l}{w}R_{\square} = jnd^2\frac{l}{w}R_{\square} = j\frac{l}{w}w^2\frac{l}{w}R_{\square} = jl^2R_{\square}} \qquad \text{(Eq. 1)}$$

As explained in section 2, the deposition ratio of volume and charge $b = 5.9 \times 10^{-11}$ m^3/C or 590 nm cm^2/C. For a typical current density $j = 2$ mA/cm^2 and 100% Faradaic efficiency (see Fig. 3), the deposition rate $k = jb = 1.2$ nm/s. That means that a typical cell is filled in 10 to 100 s. In our design and processing, the resistivity for the TiN bottom electrode is *ca.* 1.2(1) µΩ m, and with a thickness of 100 nm results in a sheet resistance of $R_{\square} = 10$ Ω. Assuming a chip size of 5 mm x 5 mm, the voltage drop can now be calculated as 5 mV. This value is small enough so as not to be a significant influence during the electrodeposition process and shows that this process has the potential to scale. It should be remarked that the above equation is very coarse with several assumptions, but even for different compositions, density, and design, the voltage drop is likely to stay below 20 mV for any feasible matrix design. In light of the long individual lines to the contact window which have afterwards been severed, open resistance between the different word lines was carefully monitored. The open resistance was always above 50 MΩ where matrices were prepared without holes demonstrating the integrity of the process and the sputtered SiO_2 isolation.

In addition to the possible effects of *iR*-drop on the electrochemistry, the uncompensated resistance can affect the transient response of the electrochemistry through its effect on the *RC* time for the electrode. For a 1 µm^2 cell, taking into account the bottom contact line resistance ($R_{contact}$) and using the specific double layer capacitance (C_{dl}) measured in the same electrolyte using a large area TiN electrode (~30 µF/cm^{-2}) the *RC* time constant is << 1 ms so that double layer charging of the electrode should not have a significant effect on the electrodeposition process in this design.

Memory matrix fabrication and characterisation

The fabrication process of the memory matrix is shown in Fig. 9 which consists of bottom electrode (BE) patterning (a-e), GST nanocell device patterning (f-i), GST electrodeposition (j), top electrode patterning (k-n) and bottom electrode contact opening (not shown). A 500 nm SiO_2 film was deposited on a Si wafer as an insulating layer by reactive sputtering of Si in an O_2 atmosphere (Fig. 9a). AZ2072 photoresist was then spin-coated onto the wafer and exposed under a UV light (EVG 620TB) to pattern the bottom electrodes (Fig. 9b). The resist development was carried out by using an AZ726 developer for 100 s and rinsing with deionised water (Fig. 9c). A single layer of 100 nm TiN was reactively sputtered (Ti target in a N_2 atmosphere) to form the bottom electrodes, connection paths and contact window for electrodeposition using a lift-off process (Fig. 9d-9e). The width *w* of the individual TiN lines is 5 µm and the connection paths were patterned in a zigzag shape to prevent any slippage due to their length during the lithography process and to suppress interconnection between them. A 200 nm SiO_2 layer is deposited by reactive sputtering to form the isolation (Fig. 9f). Individual confined cells are defined by e-beam lithography (JEOL

9300FS). E-beam resist ZEP520 was spin-coated and patterned to form cells with sizes varying from *d* = 100 nm to 1000 nm (Fig. 9g-9h). This was followed by a SiO_2 reactive ion etching in in CHF_3 and Ar (Oxford Instrument Plasmalab 80+) to reveal the TiN bottom electrode in the SiO_2 layer (Fig. 9i). After electrodeposition of GST (Fig. 9j), TiN top electrodes (TEs) were patterned with similar lithography, sputtering and lift-off processes (Fig. 9-9n) and contact windows to the bottom electrodes were exposed by another lithography process follow by SiO_2 etching. Subsequently, the connection paths were broken to isolate each bottom electrode (Fig. 9o).

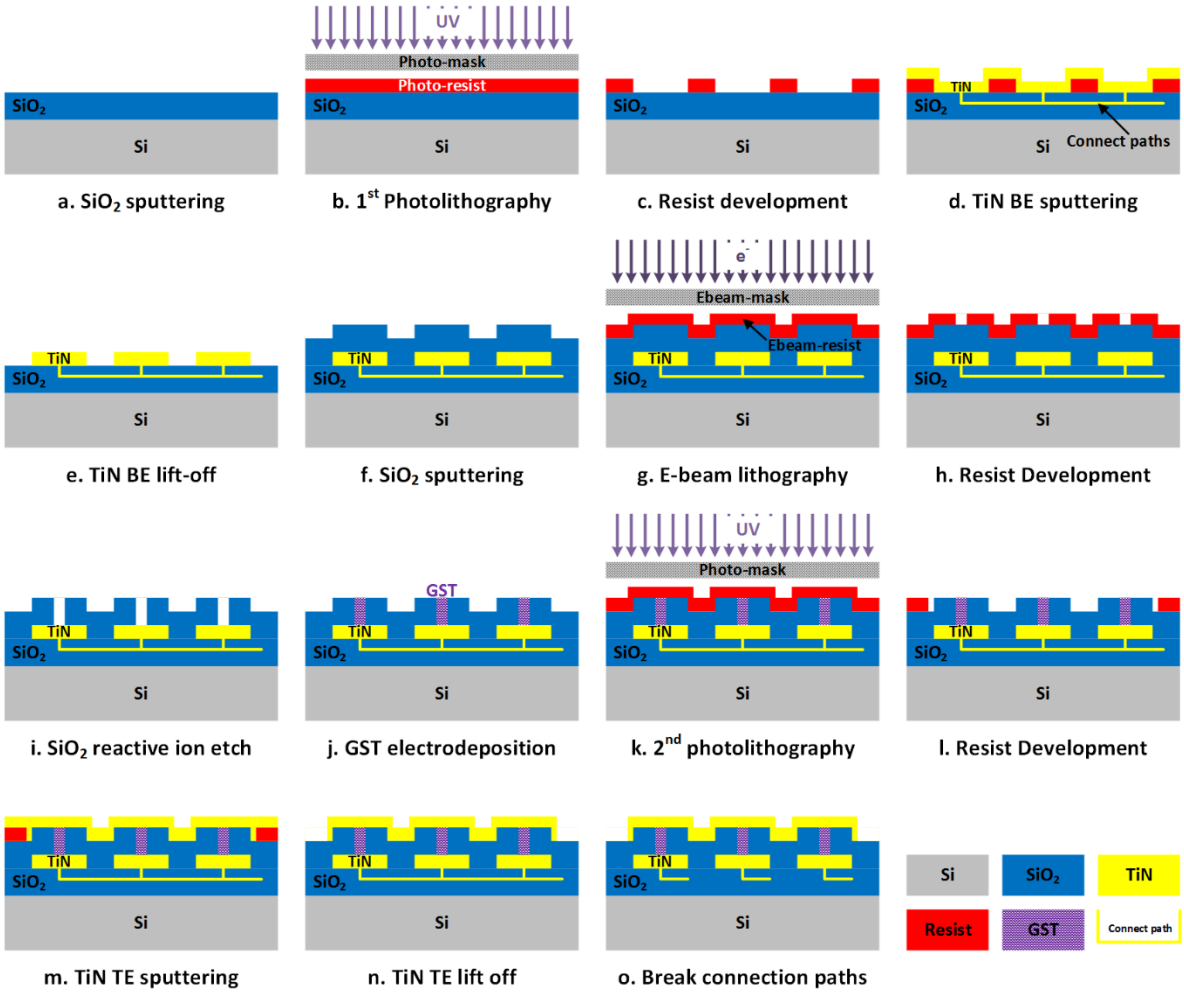

Fig. 9. Process flow for the fabrication of a passive memory matrix from electrodeposition. Descriptors of colours and elements are provided in the figure.

Fig. 10a presents SEM images of the 10 x 10 matrix after GST electrodeposition, in which every cell on the bottom electrode has been uniformly filled. Fig. 10b is a cartoon of the matrix after top electrode patterning. The optical microscopy images of the functional 10 x 10 and 1 x 10 matrix after fabrication are shown in Fig. 10c and Fig. 10d, respectively.

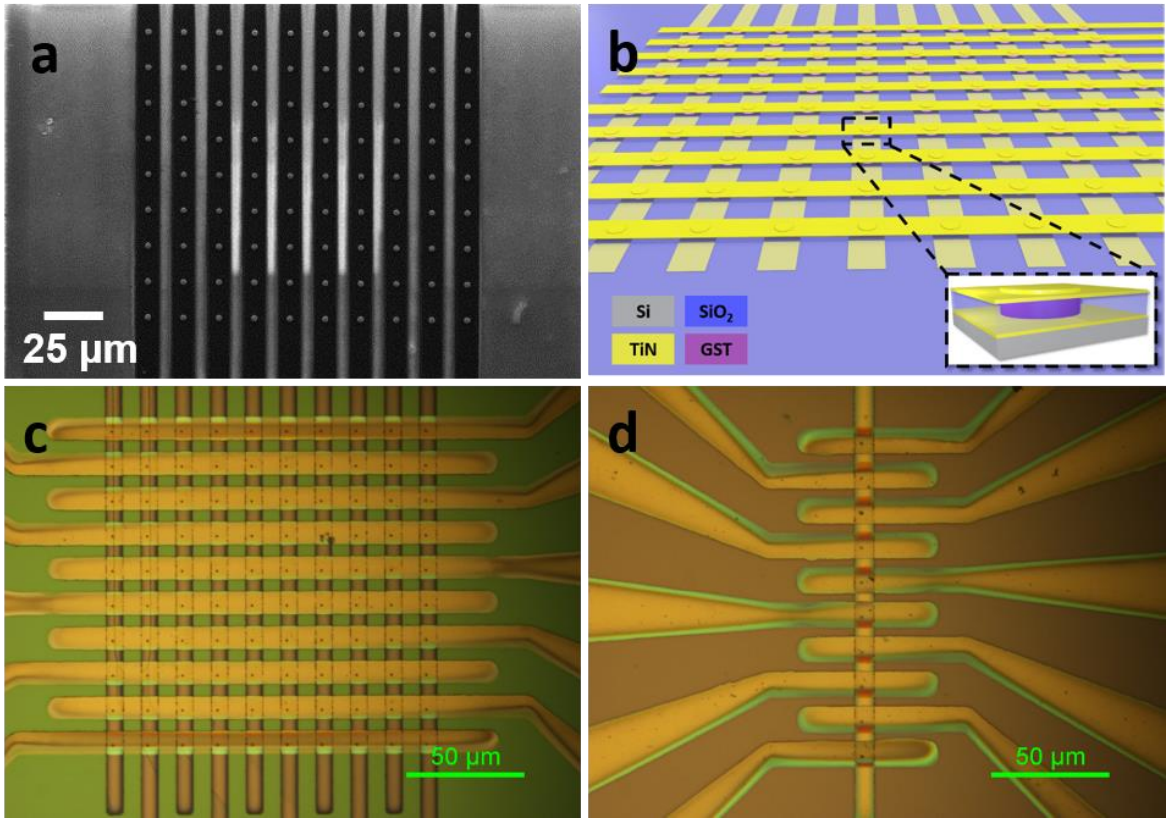

Fig. 10 (a) SEM images of the matrix after GST electrodeposition; (b) design of passive matrix suitable for electrodeposition with lithographically defined counter electrode; optical images of functional 10x10 (c) and 1x10 (d) passive matrix cells with e-beam lithography patterned confined cells.

Fig. 11 shows the electrical resistivity of the TiN bottom and top contacts. The 100 nm bottom contact as measured from the electrodeposition window to individual matrices shows an extracted resistivity of 1.2(1) µΩ m, only slightly higher than the 0.85 µΩ m for a thin TiN film. The actual resistance of up to 35 kΩ is for the matrices at the bottom of the contact lines/word lines. As the total required charge in a word line of maximum dimension cells (1000 nm x 1000 nm) is 10^{-7} C or 10^{-9} A for 100 s filling, the actual voltage drop is below 0.1 mV. The top contact resistivity is significantly larger (3.2 µΩ m) due to the roughness of the films and the distortion of the TiN line caused by underfilled or overfilled confined cells.

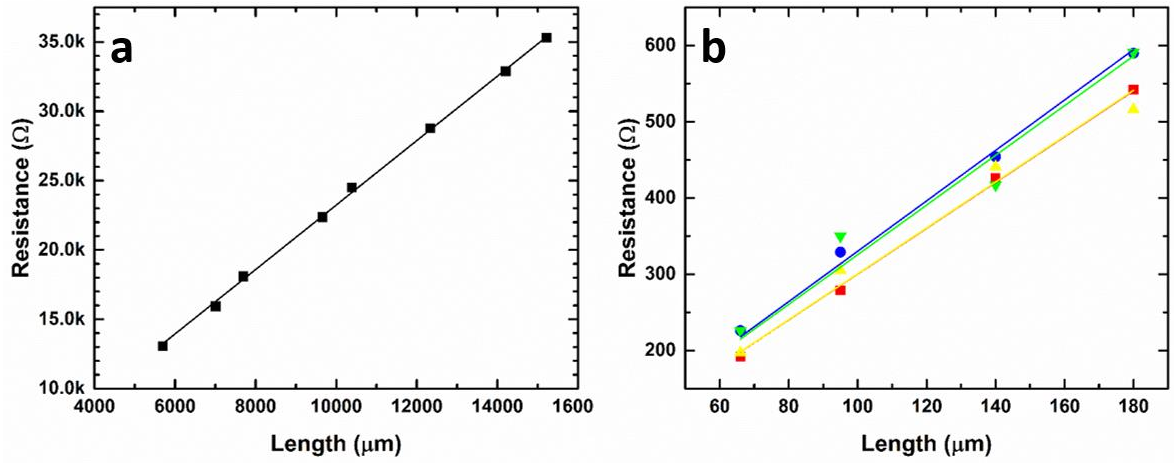

Fig. 11 (a) Resistance of 100nm TiN bottom contact lines/word lines as measured from electrodeposition pad to Ge-Sb-Te matrices across the chip. Extracted resistivity of the TiN word lone is 1.2(1) µΩ m. (b) Resistance of four different 200 nm TiN top contact/bit

lines as measured across the Ge-Sb-Te matrix pad. Extracted resistivity of the TiN bit line is 3.2 (2) μΩ m. Four-point probe resistivity of the reactively sputtered TiN is 0.85 μΩ·m.

Electrical characteristics of Ge-Sb-Te cells

Preliminary data on Ge-Sb-Te cells that were electrodeposited from an electrolyte containing 1 mM of $[NBu^n_4][GeCl_5]$, 1 mM $[NBu^n_4][SbCl_4]$ and 2 mM $[NBu^n_4]_2[TeCl_6]$ are presented in this section. The EDX compositional analysis of the 500 nm and 1000 nm cells indicate that the Sb content is around 90% for the individual cells, slightly above the concentration that was expected from the electrolyte variation experiments and the phase change memory that was reported in the first section. The resistance distribution of the individual cells (from measurements on the 10 x 1 arrays) is given in Fig. 12a. None of the devices showed phase change memory behaviour, but those devices with low pristine resistance did show resistive memory behaviour with positive bipolar switching from the pristine low resistance state to the high resistance state upon application of a potential to the top electrode. This behaviour is shown in Fig 12b. Bipolar resistive switching has been demonstrated previously in $Ge_2Sb_2Te_5$ and is shown to be caused by ionic migration leading to local depletion and species separation at bottom electrode interface.[21] Electrical characterisation on the 10 x 10 passive matrix resulted in resistance measurements consistent with those taken from individual devices on 1 x 10 arrays. However, as the matrices currently do not contain a selector and non-linear element sneak path currents are significant. Line resistance also has to be taken into account when analysing the matrices.[22]

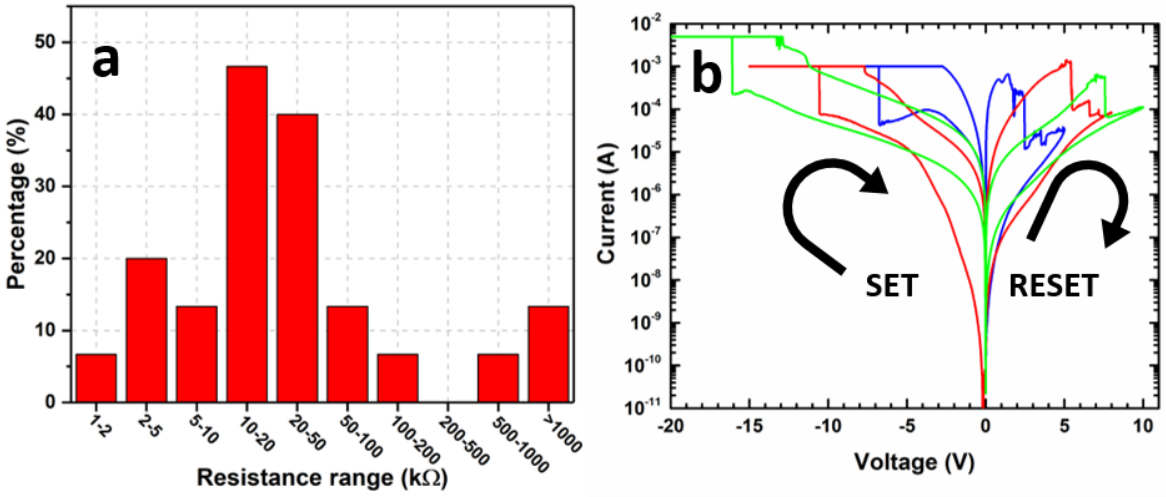

Fig. 12 (a) Resistance distribution of individual pristine cells in a 1 x 10 array for cells filled with GeSbTe; (b) I-V characteristics of an individual 1000 nm cell in a 1 x 10 array showing resistive switching behaviour.

Discussion and Conclusion

Although electrodeposition of functional semiconductors or chalcogenide memory in particular is not of similar maturity as physical vapour deposition, the possibilities for scaling and device design bring a number of advantages that may be exploited in the future. Firstly, as the composition is dependent on the electrodeposition potential, a pulsed or ramped potential could result in multilayers or gradient composition films. The level of control over the composition of electrodeposited multilayer has been demonstrated In Co/Cu multilayers for giant magneto-resistance where 2 nm layers are alternated.[23] The gradient approach would be easier to implement in Ge-Sb-Te memory. It has recently been shown that electro-migration effects are already established to a significant extent after the first 10 switching cycles.[24,25] A compositional gradient that counteracts the drift or already implements it

could reduce this effect. A second implementation of such compositional variation would be interfacial control. It has been shown previously that for films thinner than 100 nm both in the crystalline and the amorphous phase the contact resistance dominates.[26,27]

The low temperature of the electrodeposition process limits diffusion at the metal-semiconductor interface and hence allows the formation of Schottky barriers with order of magnitude lower reversed bias current than sputtering or evaporation.[28,29] If a correct implementation of PCM memory Schottky barrier can be found this would result in a build-in selector and provide the ability to efficiently scale passive matrices.[30] The last and most conspicuous advantage of electrodeposition is that it is not a line-of-sight technique. True 3D memory in which the lithographic steps do not scale with the number of layers, similar to what has been demonstrated for Flash memory has not yet been realised for novel non-volatile memory.[31] The ability to electro-deposit in lateral etched-back cavities would open up a much larger design space for such memory than can be achieved with line-of-sight techniques.

In this paper, we have shown the current state-of-the-art in electrodeposition of functional chalcogenide memory, and highlighted both the challenges and opportunities that the large parameter phase of this method provides. The key ability to deposit into high aspect-ratio cells might one day lead to mainstream electrodeposited semiconductor devices. Neuromorphic phase change or resistive memory might be the prime applications that can take advantage of this method.

Conflicts of interest

There are no conflicts to declare.

Acknowledgements

This work has been supported by the EPSRC through the Programme Grant, Advanced Devices by Electroplating (ADEPT - EP/N0354371/1), and the research grant Phase Change Memory Materials via Non-Aqueous Electrodeposition into Nano-structured Templates (EP/I010890/1). P.N.B. gratefully acknowledges receipt of a Wolfson Research Merit Award. The authors thank Dr Josephine Corsi for editorial support. All data can be found on dataset doi:10.5258/SOTON/D0601.

References

1 T. Tuma, A. Pantazi, M. Le Gallo, A. Sebastian and E. Eleftheriou, *Nat. Nanotechnol.*, 2016, **11**, 693–699.
2 G. W. Burr, R. M. Shelby, A. Sebastian, S. Kim, S. Kim, S. Sidler, K. Virwani, M. Ishii, P. Narayanan, A. Fumarola, L. L. Sanches, I. Boybat, M. Le Gallo, K. Moon, J. Woo, H. Hwang and Y. Leblebici, *Adv. Phys. X*, 2017, **2**, 89-124..
3 S. W. Fong, C. M. Neumann and H.-S. S. P. Wong, *IEEE Trans. Electron Devices*, 2017, **64**, 4374-4385.
4 A. L. Lacaita and A. Redaelli, *Microelectron. Eng.*, 2013, **109**, 351–356.
5 R.-Y. Kim, H.-G. Kim and S.-G. Yoon, *Appl. Phys. Lett.*, 2006, **89**, 102107.
6 X. Liang, N. Jayaraju and C. Thambidurai, *Chem.Mater.*, 2011,**23**, 1742–1752.
7 Q. Huang, a. J. Kellock and S. Raoux, *J. Electrochem. Soc.*, 2008, **155**, D104.
8 P. C. Andricacos, C. Uzoh, J. O. Dukovic, J. Horkans and H. Deligianni, *IBM J. Res. Dev.*, 1998, **42**, 567–574.
9 P. C. Andricacos, *Electrochem. Soc. Interface*, 1999, **8**, 32–37.
10 D. Del Frari, S. Diliberto, N. Stein, C. Boulanger and J.-M. Lecuire, *Thin Solid Films*, 2005, **483**, 44–49.
11 F. Endres, *Electrochem. Solid-State Lett.*, 2002, **5**, C38–C40.
12 P. N. Bartlett, S. L. Benjamin, C. H. (Kees) de Groot, A. L. Hector, R. Huang, A. Jolleys, G. P. Kissling, W. Levason, S. J. Pearce, G. Reid and Y. Wang, *Mater. Horiz.*, 2015, **2**, 420–426.
13 P. Noé, C. Vallée, F. Hippert, F. Fillot and J.-Y. Raty, *Semicond. Sci. Technol.*, 2018, **33**, 013002.
14 S. Guerin, B. Hayden, D. W. Hewak and C. Vian, *ACS Comb. Sci.*, 2017, **19**, 478–491.
15 P. N. Bartlett, D. Cook, C. H. (Kees) de Groot, A. L. Hector, R. Huang, A. Jolleys, G. P. Kissling, W. Levason, S. J. Pearce and G. Reid,

RSC Adv., 2013, **3**, 15645.
16 P. N. Bartlett, C. Y. Cummings, W. Levason, D. Pugh and G. Reid, *Chem. Eur. J.*, 2014, **20**, 5019–5027.
17 C. Y. Cummings, P. N. Bartlett, D. Pugh, G. Reid, W. Levason, M. M. Hasan, A. L. Hector, J. Spencer and D. C. Smith, *J. Electrochem. Soc.*, 2015, **162**, D619–D624.
18 C. G. Fink and V. M. Dokras, *J. Electrochem. Soc.*, 1949, **95**, 80.
19 R. Huang, G. P. Kissling, A. Jolleys, P. N. Bartlett, A. L. Hector, W. Levason, G. Reid and C. H. 'Kees' De Groot, *Nanoscale Res. Lett.*, 2015, **10**, 432.
20 K. Uda, Y. Seki, M. Saito, Y. Sonobe, Y. C. Hsieh, H. Takahashi, I. Terasaki and T. Homma, *Electrochim. Acta*, 2015, **153**, 515-522.
21 N. Ciocchini, M. Laudato, M. Boniardi, E. Varesi, P. Fantini, A. L. Lacaita and D. Ielmini, *Sci. Rep.*, 2016, **6**, 1–9.
22 A. Chen, *IEEE Trans. Electron Devices*, 2013, **60**, 1318–1326.
23 W. Schwarzacher and D. S. Lashmore, *IEEE Trans. Magn.*, 1996, **32**, 3133–3153.
24 W. Kim, M. Brightsky, T. Masuda, N. Sosa, S. Kim, R. Bruce, F. Carta, G. Fraczak, H. Y. Cheng, A. Ray, Y. Zhu, H. L. Lung, K. Suu and C. Lam, in *Technical Digest - International Electron Devices Meeting, IEDM*, 2016, p. 4.2.1-4.2.4.
25 Y. Xie, W. Kim, Y. Kim, S. Kim, J. Gonsalves, M. BrightSky, C. Lam, Y. Zhu and J. J. Cha, *Adv. Mater.*, 2018, **1705587**, 1705587.
26 R. Huang, K. Sun, K. S. Kiang, R. Chen, Y. Wang, B. Gholipour, D. W. Hewak and C. H. De Groot, *Semicond. Sci. Technol.*, 2014, **29**, 095003.
27 F. Xiong, E. Yalon, A. Behnam, C. M. Neumann, K. L. Grosse, S. Deshmukh and E. Pop, in *2016 IEEE International Electron Devices Meeting (IEDM)*, IEEE, 2016, p. 4.1.1-4.1.4.
28 M. E. Kiziroglou, A. A. Zhukov, X. Li, D. C. Gonzalez, P. A. J. de Groot, P. N. Bartlett and C. H. de Groot, *Solid State Commun.*, 2006, **140**, 508–513.
29 M. K. Husain, X. Li and C. H. De Groot, *Electron Devices IEEE Trans.*, 2009, **56**, 499–504.
30 A. Velea, K. Opsomer, W. Devulder, J. Dumortier, J. Fan, C. Detavernier, M. Jurczak and B. Govoreanu, *Sci. Rep.*, 2017, **7**, 8103.
31 K. T. Park, S. Nam, D. Kim, P. Kwak, D. Lee, Y. H. Choi, M. H. Choi, D. H. Kwak, D. H. Kim, M. S. Kim, H. W. Park, S. W. Shim, K. M. Kang, S. W. Park, K. Lee, H. J. Yoon, K. Ko, D. K. Shim, Y. Lo Ahn, J. Ryu, D. Kim, K. Yun, J. Kwon, S. Shin, D. S. Byeon, K. Choi, J. M. Han, K. H. Kyung, J. H. Choi and K. Kim, *IEEE J. Solid-State Circuits*, 2015, **50**, 204–213.

